Particle loss mitigation in asphalt by the addition of polyethylene foam

M. Abedraba-Abdalla [a,*], Nick Thom [a], A. Garcia-Hernández [b], Linglin Li [a]

[a] *Nottingham Transportation Engineering Centre, Department of Civil Engineering, University of Nottingham, Nottingham NG7 2RD, United Kingdom*
[b] *Lehrstuhl und Institut für Straßenwesen, Aachen University, Aachen 52074, Germany*

A B S T R A C T

This paper evaluates the feasibility of using a cellular foam as a substitute for capsules containing rejuvenators to mitigate the ravelling of Stone Mastic Asphalt and enhance its durability. While encapsulated rejuvenators have been shown to effectively release the rejuvenator and partially restore asphalt viscosity, recent research has found that the capsules exhibited a porous structure that has a non-negligible effect on the arrangement of the aggregate skeleton in SMA mixtures, which might impact the asphalt performance in mitigating ravelling by absorbing the energy from the external loads. To address this, a Polyethylene Terephthalate (PET) foam with three different densities is used in this study to assess the effect of an energy-absorbing cellular structure on asphalt performance and ravelling mitigation. Mechanical tests have been conducted on SMA mixtures containing 1 % and 5 % of the total volume of the mixture to determine the resistance to rutting, fatigue and particle loss. Results indicate that foam density influences particle loss and rutting resistance, with higher foam content enhancing fatigue life. Moreover, all foam types exhibit improved surface ravelling resistance, suggesting that integrating porous particles with inherent energy absorption capabilities could enhance SMA mixture durability.

1. Introduction

Stone Mastic Asphalt (SMA) mixtures are gap-graded with a coarse aggregate skeleton and high filler and asphalt binder contents [1], [2]. The purpose behind the gap gradation of crushed aggregate is to increase pavement stability via stone-to-stone contact gripped together through a strong mix of filler and other additives [3]. Typical applications of SMA surface in the UK include heavily trafficked and high-speed roads due to its high anti-rutting performance [4]. However, further research is required to determine the design of the aggregate structure to maximise the performance of stone-to-stone contact and to understand the relation between the aggregate structure and the mixture properties [5], [6].

SMA mixtures are prone to ravelling because of the interconnected voids and high stresses concentrated on stone-to-stone contacts, which can result in cohesive and/or adhesive failure [7], [8]. It is a mixture-associated defect in which the loosening of coarse aggregates from the surface layer occurs because of the shear stresses generated from tyre movement, particularly during driving manoeuvres [8], [9], [10]. In pavement engineering, there have been many approaches to treating ravelling resistance, including altering the rheological properties or replacing part of the aggregate-mastic skeleton [11].

Polymer-modified bitumen, for instance, enhances adhesion between bitumen and aggregate at lower temperatures, however asphaltene content has a stronger effect on adhesion than bitumen modification [12]. Both organic polymer and inorganic substrates can also improve adhesion between the materials [13]. These additives are most effective at lower temperatures and address minor factors contributing to ravelling compared to bitumen aging, mechanical loading, and aggregate interaction [14].

In recent years, rejuvenation methods through sunflower oil encapsulated particles have been developed to increase the self-healing potential of oxidised and aged bitumen by re-establishing the natural ratio of solid particles to oils and resins [15]. The potential enhancement of ravelling resistance through bitumen healing lies in the restoration of the ability of the bitumen to flow, enabling the closure of the microcracks [16], [17], [18], [19], [20], [21]. However, in recent studies focusing on testing asphalt containing encapsulated rejuvenators [16] under impact loading to assess its resistance to abrasion through the Cantabro test [22], [23], it was concluded that the reduction observed could not be ascribed to a self-healing mechanism since there were no resting periods applied to allow the diffusion and promotion of oil by the rejuvenator. Consequently, this mitigation was attributed to the capsules' internal porous structure and the cells' ability to absorb energy

while gradually collapsing. Further research studied the influence of various variables during asphalt manufacturing on the energy absorption of the capsules in SMA mixtures produced at an asphalt plant, and the derived conclusion stated that for optimal effectiveness of the capsules, they should be integrated into the aggregate skeleton instead of floating within the mastic [24].

These findings suggested researching an alternative to encapsulated rejuvenators' by looking into materials with mechanical responses solely defined by their porous structure. This is to minimise the variables influencing the encapsulated rejuvenators and determine whether the observed outcomes in previous studies should be attributed to energy absorption of the cellular structure of the capsules. This structural configuration, encompassing foams, meshes, and micro lattices [25], [26], is used in several biological systems, including honeycomb, wood, and cork. The material's porous structure provides a unique but desirable combination of lightweight [27] and strength, and its mechanical properties can be tailored to fulfil specific needs [26], [28]. For instance, energy absorption efficiency might be adjusted by selecting the right material, designing the cells, controlling the material thickness, and adjusting the porosity [29].

Under loading, polymer foams follow a stress-strain behaviour characterised by a long plateau region corresponding to large plastic deformation, in which a significant amount of energy is expected to be completely dissipated [30], [31]. Foams can be broadly classified as closed-cell and open-cell structures. Closed-cell foams tend to be more rigid and have higher compressive strength [33]. A variety of closed-cell polymer foams with varied structural designs, including tubes, sandwiches [32], [33], and plates [34] have been widely used in the automobile, railway, construction, and aerospace industries [35]. However, no previous studies have employed polymeric cellular foam in asphalt to evaluate the effect of their porous structure and the intrinsic energy absorption characteristic in enhancing asphalt ravelling.

Hence to study the effect of energy absorbing foams and their densities in delaying asphalt ravelling, this research used a commercially available Polyethylene Terephthalate (PET) foam core with three different densities 130, 200 and 320 kg/m^3 that withstands temperatures higher than 165°C and presents good mechanical characteristics to be mixed with asphalt. The three types of foam were mixed with asphalt at 1 % and 5 % of the total volume of asphalt mixture to study the influence of foam content on asphalt performance. Asphalt mixtures were manufactured to assess the stiffness, rutting, particles loss, fatigue, and wear resistance, using the Indirect Tensile Stiffness Modulus (ITSM), Hamburg Wheel tracker, Cantabro test, Indirect Tensile Fatigue Test (ITFT), and the scuffing test. The inclusion of foam yielded similar results to the encapsulated porous particles, indicating that the physical effect might impact asphalt performance by creating a different aggregate arrangement, resulting in a distinct stone-to-stone contact where the foam absorbs the energy from external loads, mitigating the potential dislodgment and loss of the aggregates.

2. Materials and methods

2.1. Experimental work

The experiments designed in this study were as follows:

1) Characterise the mechanical properties of the three types of foam to determine the energy absorption characteristics.
2) Perform aggregate loss test using the Cantabro machine on asphalt mixtures with 1 %, 3 %, 4 %, and 5 % of the total volume of the mixture.
3) Based on the results from the Cantabro and the availability of T92 foam, only 2 percentages, 1 % and 5 %, were used for the remaining experimental tests which included: volumetrics, rutting resistance, stiffness modulus and wear resistance.

2.2. Selection and sample preparation of polymer foam

This study used commercially available and high-performance structural polymeric foams called Airex-T92. The cross-linked closed-cell Polyethylene Terephthalate (PET) foam manufactured by a high-pressure nitrogen gas solution process was produced by 3 A Composite Core Materials and provided by Trident. Specifically, three variants of closed-cell thermoplastic and recyclable T92 foam, Airex T92.130, T92.200 and T92.320, with nominal densities of 130 kg/m^3, 200 kg/m^3 and 320 kg/m^3, respectively, were selected due to their mechanical characteristics, which enable them to perform effectively in environments exposed to high temperatures, and fatigue requirements [36]. 3 A Composites Core Material reported the mechanical properties of Airex T92 and asserted that they are designed to meet the needs of very highly loaded applications with their high strength, stiffness, and fatigue resistance [36].

The samples were provided in the form of 4 m x 4 m x 0.005 m sheets. Subsequently, these sheets were precisely sectioned via a saw-cutting process at the University of Nottingham to yield beam sheets with dimensions of 4 m x 0.005 m x 0.005 m. These beam sheets were manually further sectioned using sharp blades into small 5 mm cubes for subsequent analysis, as this was visually deemed by the authors to be the smallest sample size that maintained the integrity of the pores within the sample. See Fig. 1 showing T92.200 foam manually cut into 5 mm cubes. The foam size and content in the asphalt mixture were derived from prior research on encapsulated porous particles [23], [24], [37], [38], [39], [40]

2.3. Asphalt mixture and manufacturing procedure

Stone Mastic Asphalt (Ultrapave 10 surf), in accordance with EN 13108 Part 5, a material commonly used to build surface courses on roads in the UK, was manufactured with 0 %, 1 %, 3 %, 4 % and 5 % of Airex T92.130, T92.200 and T92.320 (melting point: 240°) by the total volume of the mixture. 1 % of the total mix volume was selected from previous literature [23] that determined that it is the optimum content for 1.6 mm energy-absorbing particles to increase asphalt durability. To calculate the total volume of the foam, the mass percentage of the capsules is first converted to a volume percentage based on the maximum mass of asphalt and the density of the capsules. This volume percentage is then used to estimate the foam volume using the maximum asphalt volume, determined from the maximum density (2551 kg/m^3) and mass of the mixture without foam. The materials used were gritstone aggregates (2.800 g/cm^3), granite dust (2.670 g/cm^3), cellulose fibre (0.095 g/cm^3) and 40/60 pen bitumen (1.027 g/cm^3). The mixture was composed of 15 % of granite dust, 16 % of 6 mm gritstone, 48.4 % of 10 mm gritstone, 5 % of 14 mm gritstone, 8.5 % filler, 0.3 % fibre and 6.4 % binder content by total weight of the mixture. The target air void is 3 % and the maximum targeted volume is 0.0045 m^3. A total of 16 asphalt slabs were manufactured, with an average weight and height of 11448 ± 2 g and 50 mm, respectively. In addition, 60 asphalt cores were prepared in groups of 5 samples of 150 mm diameter, averaging 1128 g in weight and 60 mm in height. Aggregates and bitumen were preheated at 165°C for 6 and 4 h, respectively. For both slab and core manufacturing, the mixture procedure and time of adding the foam was done following [23], [39]

The assessment of bulk density, ρ_b in asphalt mixtures, both with and without T92 foam, was carried out in accordance with British standard BS EN 12697–6:2020. To calculate ρ_b, the mass of the dry specimen was divided by the difference between its mass in air and water and then multiplied by the density of water at ambient temperature. Furthermore, the air void content (V_a) in the asphalt mixture was determined using bulk density measurements and the maximum theoretical density according to BS EN 12697–8: 2018 [41]. The maximum theoretical density was calculated analytically, including the foam density, according to BS EN 12697–5: 2009 [42].

Fig. 1. Illustration of T92.200 foam manually cut into 5 mm cubes for analysis and mixing with asphalt.

2.4. Foam morphological characterisation

The quantitative study of cellular material structure, properties, and mechanical response is mostly limited to cell diameter, cell topology, and the relative density of the foam material, the density being the most substantial parameter that describes a mechanical characteristic of the foam morphology [43], [44]. The relative density of the foam material (ρ^*) is an expression of the solid fraction, and it is given by Eq. (1) in accordance with ASTM D3575 as follows:

$$\rho^* = \frac{\rho_f}{\rho_p} \tag{1}$$

where ρ^* is the relative density of the foam, ρ_f is the foam density, and ρ_p is the polymer density, with the latter being approximated as 952 kg/m^3, which falls within the density range of PET materials reported in the literature [45] [46]. The relative densities for the specific foam variants, T92.130, T92.200 and T92.320, are 0.14, 0.2, and 0.33, respectively. Greater relative density is generally attributed to higher proportions of bulk material within the foam [30]. Moreover, the morphology investigation of foams is typically conducted in two dimensions [44], [47]. The internal structure of the foams was examined using a light microscope (Nikon Eclipse LV100ND) equipped with TU Plan Fluor EPI lenses and a 4080 × 3120-pixel colour sensor. The images obtained at a magnification of x5 were used to determine the pore size and porosity of the foams. For each sample, three sections were evaluated, covering an area of 25 mm^2 per section. Image analysis was performed using automated image thresholding coupled with morphological segmentation in ImageJ software to calculate the cell dimension and the porosity. Given the irregular nature of cells, the diameter was defined as the maximum diameter between vertices [44], [48].

2.5. Distribution of foam in asphalt

X-ray Computed tomography scanning was utilised to analyse the distribution and deformation of foam within the asphalt with a Phoenix Vtomex M scanning device produced at Waygate Technologies, Germany. The device operated at 200 kV and has 40 µm spatial resolution. To assess any changes in the morphology of the foam post asphalt manufacturing and to inspect its resistance to the mixing process, two

cylindrical cores with 5 % T92.130 and T92.320 of 60 mm height and 40 mm diameter were extracted from a manufactured slab prior to testing. Additionally, two cores of 40 mm in height and 70 mm in diameter were extracted from a wheel-tracked slab to assess any changes in the foam's shape. Following the data acquisition, the scans were processed and constructed using VGStudio MAX (version 2023.2) and ImageJ (version 1.41) software. The assessment was conducted considering the initial and undamaged foam volume average prior to mixing, which is 125 mm^3.

2.6. Foam mechanical properties and energy absorption

The mechanical response of individual T92 foam pieces was evaluated through uniaxial compression testing using an Instron device (5969). Cubic foam samples were subjected to 0.5 mm/min loading rate. The specimens were carefully cut using a blade knife to ensure accurate and straight cuts of 5 mm x 5 mm x 5 mm. Three specimens from each set were tested at a temperature of 20° C with the foams compressed between two steel loading platens. Compressive stress-strain curves were obtained by dividing the applied load by the initial specimen area and calculating strain as displacement divided by the original height. An optical extensometer was employed to precisely measure strain height and contact area between the steel plate and foam material.

Energy absorption was also obtained from the test results and was calculated up to the start of the densification region, a point visually identified from the curve. The calculation involved determining the area underneath the stress-strain curve, representing the absorbed energy W between two strain levels, as defined in Eq. (2):

$$W = \int_{\varepsilon_0}^{\varepsilon_f} \sigma(e)de \tag{2}$$

[49] proposed to use the energy efficiency (*E*) to evaluate the energy absorption characteristics of foam materials. Energy efficiency is when the absorbed energy at ε_f is divided by $\sigma(\varepsilon_f)$; it is obtained with Eq. (3) as shown below:

$$E = \frac{\int_{\varepsilon_0}^{\varepsilon_f} \sigma(e)de}{\sigma(\varepsilon_f)} \tag{3}$$

where ε_0, ε_f and $\sigma(\varepsilon_f)$ are the initial and final arbitrary strain and its corresponding stress. This formula expresses the ratio of the energy

absorbed by the foam to the applied stress, which is usually used to determine the optimum energy absorption working state for a given foam [50], [51].

2.7. Rut depth test

The resistance to rutting development was determined by testing asphalt slabs in the Hamburg Wheel Tracker Test (HWTT), following BS EN 12697–22 [52]. Each 305 x 305 x 50 mm^3 specimen was prepared using a roller compactor and, after demoulding, was immersed in water at 45 ± 1 °C for 8 hours to precondition. Specimens were tracked by a 55 mm wide wheel at 26.5 load cycles per minute and a load of 705 ± 4.5 N for 10,000 cycles or until a rut depth of 20 mm was reached. The rut depth was determined by averaging the measurements taken in the centre of the slab's loading area, and the proportional rut depth (%) at cycle n $(PRD)_n$ was calculated using Eq. (4), where t is specimen thickness in millimetres, r_n the vertical displacement after n cycles (mm) and r_0 the initial displacement (mm).

$$PRD_n(\%) = 100 \frac{r_n - r_0}{t} \tag{4}$$

2.8. Stiffness modulus test

To determine the Indirect Tensile Stiffness Modulus (ITSM) in accordance with BS EN 12697–26 [53], a Cooper Universal Testing Machine UTM (NU-10) was used. The test samples were preconditioned for 4 hours at two different temperatures (10 °C and 20 °C). The horizontal displacement was measured using two oppositely positioned Linear Variable Differential Transformers (LVDTs). The test procedure was repeated across two perpendicular diameters and the measured average stiffness modulus of the test pulses from the two tested diameters was recorded as the stiffness modulus of the specimen and obtained through Eq. (5), in which F, v, z and h correspond to peak value of the applied vertical load in Newtons, Poisson's ratio, the amplitude of the horizontal deformation in mm and, the mean thickness of the specimen in mm, respectively.

$$S_m = \frac{F \quad \times \quad (v + 0.27)}{(z \times h)} \tag{5}$$

2.9. Aggregate loss test

Asphalt mass loss was characterised using the Cantabro test, conducted in a Los Angeles abrasion machine in compliance with BS EN 12697–17 [54]. This test was used to evaluate and quantify the influence of 1 %, 3 %, 4 % and 5 % of T92 foam on asphalt's aggregate loss. Five samples of T92.130, T92.200 & T92.320 were tested. Before testing, samples were conditioned for 24 hours at 20 °C, then weighed, and introduced into a Los Angeles machine. The samples were subjected to a total of 300 cycles, after which the samples' weights were recorded again. Lastly, the mass loss (ML) was then estimated using Eq. (6), where M_i is the initial sample mass and M is the sample mass after 300 cycles. Before and after testing, samples were photographed to examine the change in core shape.

$$ML(\%) = 100 \frac{M_i - M}{M_i} \tag{6}$$

2.10. Fatigue test

The behaviour of the bituminous mixtures under repeated load was evaluated through an indirect tensile fatigue test using the same machine as an ITSM. This test was conducted in accordance with EN 12697–24–2018 Annex E by repeatedly applying a haversine loading of 0.1 seconds with 0.4 second resting period through the vertical diametral plane. The test was carried out in a controlled stress mode, with a single horizontal stress value of 650 kPa[55]. The controlled temperature was 10°C. The test's primary objective is to determine the fatigue life, defined as the total number of load cycles before the fracture of the specimen occurs for samples with 0 %, 1 % and 5 % of T92 foam. The specimens were conditioned for 4 hours prior to testing. The permanent deformation was determined as the accumulation of irrecoverable deformation, for each loading pulse.

2.11. Abrasion test

To measure asphalt mass loss from the surface, the scuffing wheel test was adopted to indicate asphalt's resistance to ravelling. The test consists of a loaded wheel that bears on a specimen held on a moving table with the axle of the wheel held at an angle of 20 ± 1 degrees to the vertical plane perpendicular to the direction of travel. The test follows the TRL report, Appendix G (Test procedure for scuffing) [56]. Two slabs were manufactured for each material and cut in equal halves of 305 x 152.5 x 50 mm^3 for repeatability. The samples were conditioned and tested at 30°C, a deliberately lower temperature than the standardized condition, to extend the test duration and augment the surface loss effect without compromising the integrity of the sample under loading conditions of 520 ± 5 N and an average contact pressure of 310 ± 10 kPa. The pneumatic tyre was inflated to 312 kPa and if the ribbed tread became less than 1 mm the wheel was changed.

A total of 2800 cycles was achieved for each tested sample. Each cycle consists of a translation movement with the angled wheel in the horizontal plane, with the tyres simulating the mechanical effect of vehicles when they are turning. The testing procedure was divided into sets, with the first four sets lasting 15 minutes and the last three sets lasting 30 minutes. Each set is structured in intervals, with the wheel running for 312 cycles (approximately 15 minutes) followed by a pause for sample removal, de-moulding, removal of loose material from the surface with a vacuum, slab weighing and Mean Profile Depth measurement using an Ames Laser Texture Scanner 9400. After that, the sample was reinserted for another set of cycles of 15- or 30-minutes duration. A total of 4 samples were tested for each material. The test equipment is depicted in Fig. 2.

3. Results and discussion

3.1. Foam morphological characteristics

Fig. 3(a) shows the three different foams, T92.130, T92.200 and T92.320, sectioned manually in 5 mm cubes and their inner closed-cell structure. In Fig. 3(b), foam observations by a light microscope show a 2D inner cell morphology and size. In the three density types, the inner structure comprises dense cells enclosed by walls, appears non-uniform geometrically and is shown to have a polyhedral structure. In the three materials, cell sizes exhibit uniformity with topological disorders and random orientation in all directions, which align with attributes associated with isotropic materials, as explained in previous studies [48], [57]. From the microscope examination, the cell shape appears consistent, albeit with size variations, particularly the denser material, T92.320, exhibiting smaller cell sizes than T92.130 and T92.200. Analysing the images through morphological segmentation using ImageJ allowed the estimation of cell size and area distribution. Fig. 4 shows the cell size distribution of multiple locations of each sample, with a minimum of 200 cells measured in each assembled image, to ensure a representative description. It is clear from Fig. 4 that the peak frequencies of cell size for T92.130, T92.200, and T92.320 correspond to cells sized between 0.3 and 0.4 mm, 0.2–0.3 mm, and 0.1–0.2 mm, respectively. The mean cell size, d, is obtained using Equation (7):

$$d = \frac{1}{n} \sum_{i=1}^{n} d_i \tag{7}$$
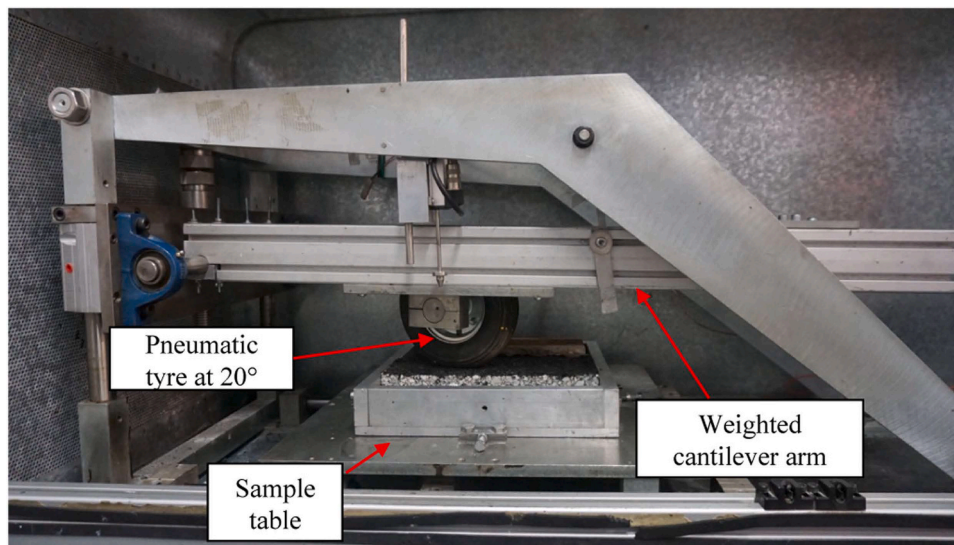
Fig. 2. Scuffing machine at NTEC.

where d_i is the size of cell, i and n is the total number of cells. The mean cell diameters of the three materials are 0.374 mm, 0.247 mm, and 0.114 mm, respectively, being classified as mesocellular structures >100 μm [31], [58]. The observed variations in cell dimensions within the three materials can be attributed to the cross-linking blowing agent and its concentration, which influence bubble expansion and formation during the foaming process[59], [60]. Specifically, increasing blowing agents generates more gas production, leading to lower foam density, evidenced by the formation of larger cells and thinner walls, which reduces material per unit volume and decreases the foam's resistance to compression [61], [62]

3.2. Assessment of mechanical properties and energy absorption

The evaluation of the mechanical properties of the foam focused on the main attributes that characterise the stress and strain curve, which are plotted in Fig. 5 and Fig. 6 alongside their energy efficiency curve in Fig. 7, and the influence of foam density on its mechanical properties is discussed. By examining the stress and strain curves of the three materials at a fixed 0.5 mm/s strain rate, it becomes evident in Fig. 5 that these curves exhibit distinct regions, consistent with descriptions found in the existing literature on cellular materials under compressive load [26], [28], [63]. The first region corresponds to the linear elastic behaviour, which occurs at strain levels of less than 5 %, 8 %, and 10 % with a slope equivalent to the foam's Young's modulus of 15.2 MPa, 25.08 MPa and 41.05 MPa for T92.130, T92.200, and T92.320, respectively, up to the peak stress where softening begins.

The subsequent stage is characterised by a plateau region representing plastic deformation [28]. Following this point, densification occurs as most cells have collapsed and opposing cells come into contact, resulting in complete compaction of the material and a sharp increase in stress observed on the stress-strain curve, at values of approximately 92 %, 85 %, and 77 % strain for 130, 200 and 320 kg/mm³. Fig. 6 shows an illustration of foam damage at different stages during the test. In examining these results, it becomes apparent that a lower density decreases slope and Young's modulus. The plateau region begins at a lower stress level with greater elongation, and densification is achieved at a much higher strain. Conversely, higher material density increases Young's modulus, and the plateau occurs at higher stress levels; however, compressive strain remains partially utilised. The three types of cellular structure foam aim to dissipate the load's energy while keeping the maximum force below the plateau stress level [28].

To better understand this, Fig. 5(a) also shows the stress required to obtain the same area under the curve, corresponding to a chosen amount of energy absorbed (11.38 J/mm³) for all densities. This amount corresponds to the selected strain from the curve where T92.130 enters densification (92 %). By comparing the stresses for, T92.130, T92.200 & T92.320, $\sigma_1(10.42 MPa)$, σ_2 (4.22 MPa), $\sigma_3(5.8 MPa)$, respectively, it can be seen that the lighter foam requires more deformation and lower stress to absorb the energy, whereas the heavier foam absorbs it with minimal deformation but experiences high-stress values. By plotting the maximum stresses reached by the three foams, as seen in Fig. 5(b), it is possible to say that a foam with intermediate density, 200 kg/m³, strikes a balance. Table 1 presents the mean value of Young's modulus, peak stress, peak strain, and plateau stress of 5 samples for each foam type.

The absorbed energy under the stress–strain curve is also calculated and plotted as a function of strain. As seen in the energy absorption in Fig. 7(a), the absorption increases as the strain increases, which occurs as the material undergoes more deformation. By plotting the efficiency, it is possible to observe the changes in efficiency ratio across varying strain levels and identify the domain where efficiency is at its peak. For the three densities, the energy efficiency exhibits a consistent pattern, as depicted in Fig. 7(b), with minimal energy absorbed in the elastic region, followed by subsequent efficiency increase reaching a peak at stresses of 1.13 MPa, 2.40 MPa and 4.24 MPa for T92.130, T92.200 and T92.320, respectively. The efficiency reaches maxima of 1.85, 1.57, and 1.55 for the three materials, and beyond that stress level, the energy efficiency diminishes with an increase in stress.

As illustrated in Fig. 7(b), the lowest and highest foam density, T92.130 and T92.320, respectively, attain the highest stress values denoted as $\sigma_1(10.42 MPa)$, $\sigma_2(5.08 MPa)$, whereas the one in between, T92.200, generates the lowest stress value $\sigma_3(4,22 MPa)$ to achieve the selected specific amount of energy (11.38 J/mm³). These findings indicate that the ideal foam within the three-density range lies between T92.130 and T92.320. Consistent with previous researchers, Linul et al. [64] documented the significance of the efficiency diagram in foam selection, and the outcome of their results involving various foams was that foam with a density in between maximum and minimum density values, necessitated the lowest stress level to obtain the same energy absorption across the selected foams, suggesting that the region of maximum efficiency might not only be controlled by the density but also by the material type and the pore size.

3.3. Assessment of the foam state after asphalt manufacturing and testing

As presented in Fig. 8, along with image analysis and foam
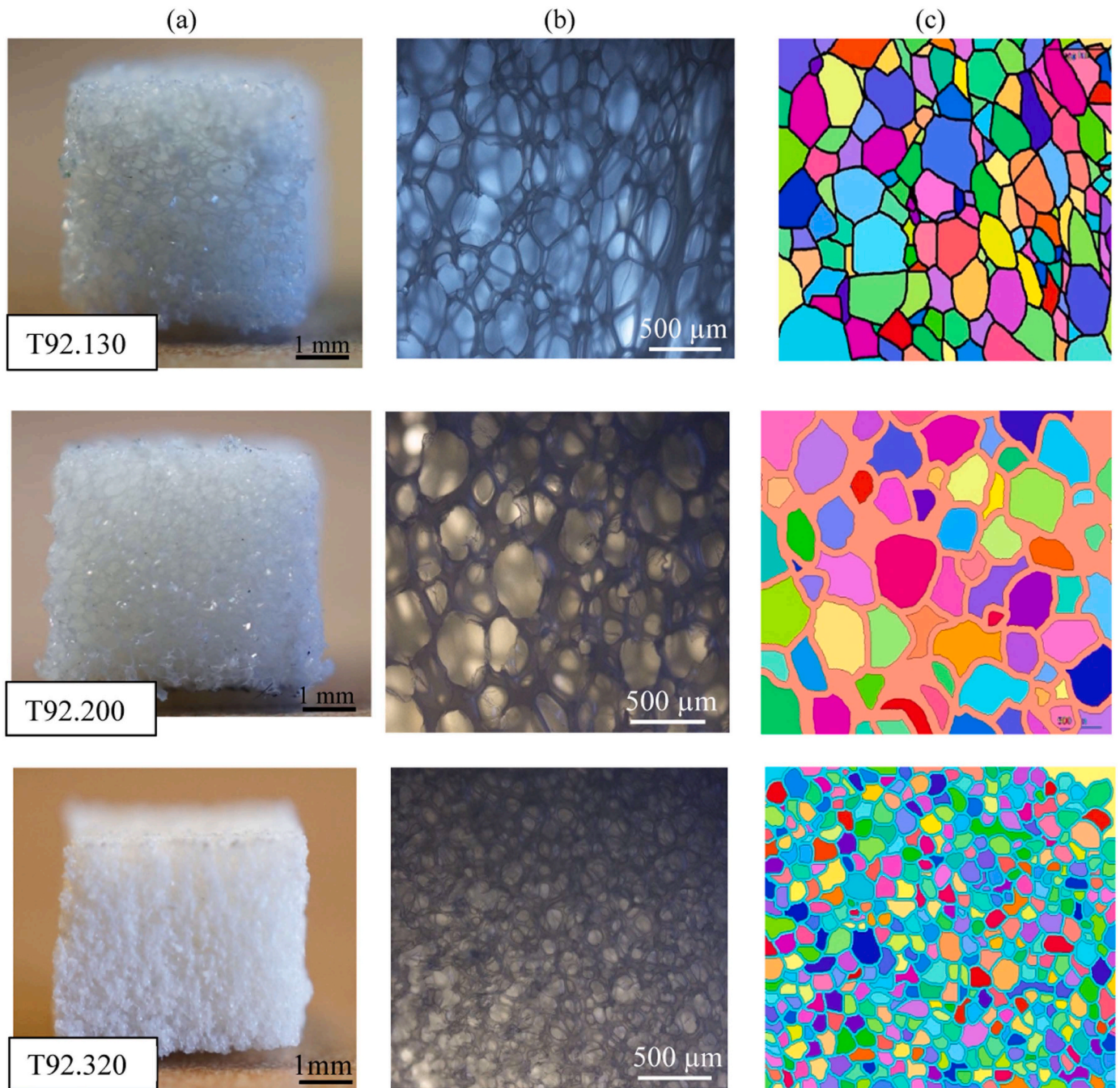
Fig. 3. (a) Outer structure of T92 (b) inner structure of T92 (c) Morphological segmentation analysis of microscopic images.

reconstruction, the results revealed height reductions of 24.64 ± 0.3 %, 21.52 ± 0.2 % and 16.94 ± 0.2 %, with volumes averaging around 94.20 ± 0.3 mm³ for T92.130, 98.10 ± 0.3 mm³ for T92.200 and 103.82 ± 0.1 mm³ for T92.320. This suggests that the foam underwent some deformation during the manufacturing and compaction process due to the rearrangement of aggregates around them. No abraded regions or fragmentation of the foam into pieces were observed in the scan.

Furthermore, to evaluate the deformation of the foam after subjecting asphalt to external loading, core specimens were extracted from tracked slabs incorporating 5 % T92.200. Illustrated in Fig. 9(a), CT scans revealed surface deformation of the core and deformation of the foam, particularly in the contact area with aggregates. The foams predominantly experienced higher deformation in the upper part of the core

closer to the surface, where foam height was reduced on average by 35 ± 5 %. According to the foam compression stress-strain data, this reduction corresponds to the strain levels identified in the plateau region. This implies that during the asphalt's exposure to the wheel tracker test, the foam cells started collapsing, which deformed the foam while absorbing energy, contributing to increased asphalt compaction levels. These findings align with Traseira et al. [23], who documented the adaptation of the shape of architected energy-absorbing particles ("capsules") to the surrounding aggregates after the Cantabro impact test.

In addition, as seen in Fig. 9, a reconstruction of a deformed foam particle and the surrounding areas is presented to illustrate the interaction of the foam with the aggregates and the mastic prior to testing the asphalt. The three aggregates, measuring 4 mm and 10 mm,
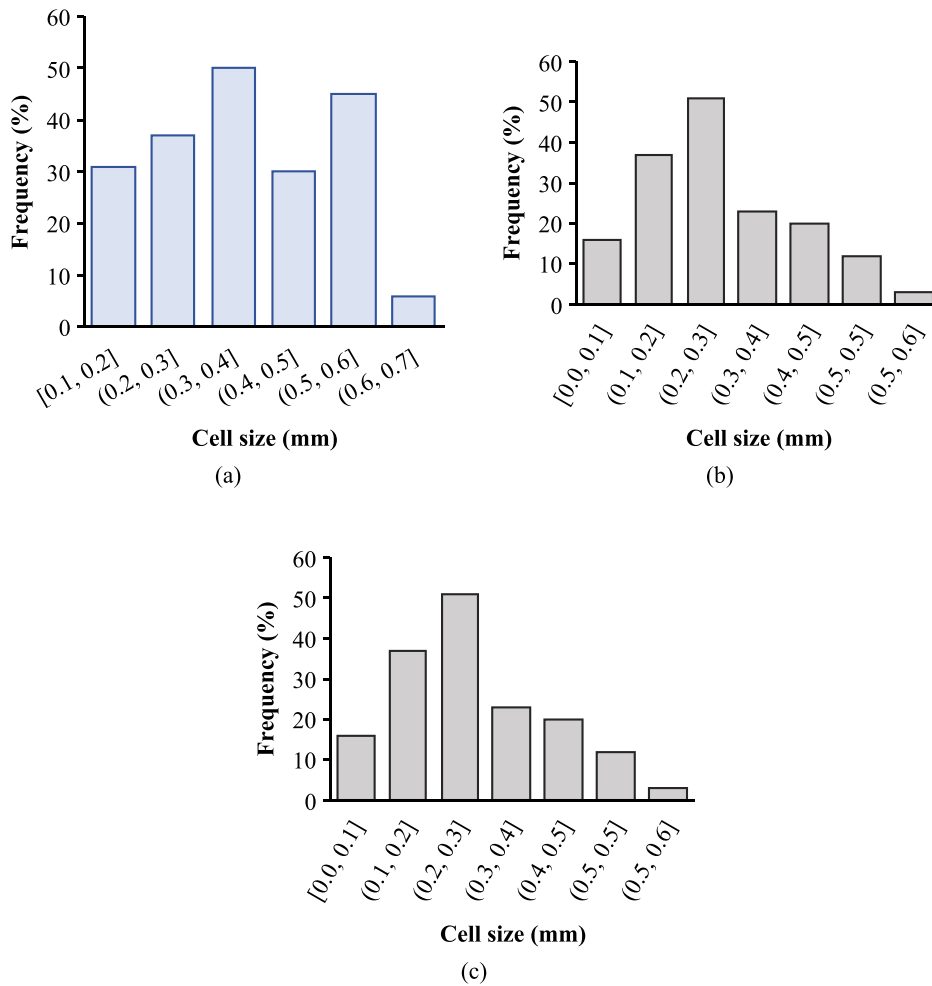
Fig. 4. (a) T92.130 cell size distribution (b) T92.200 (c) T92.320.
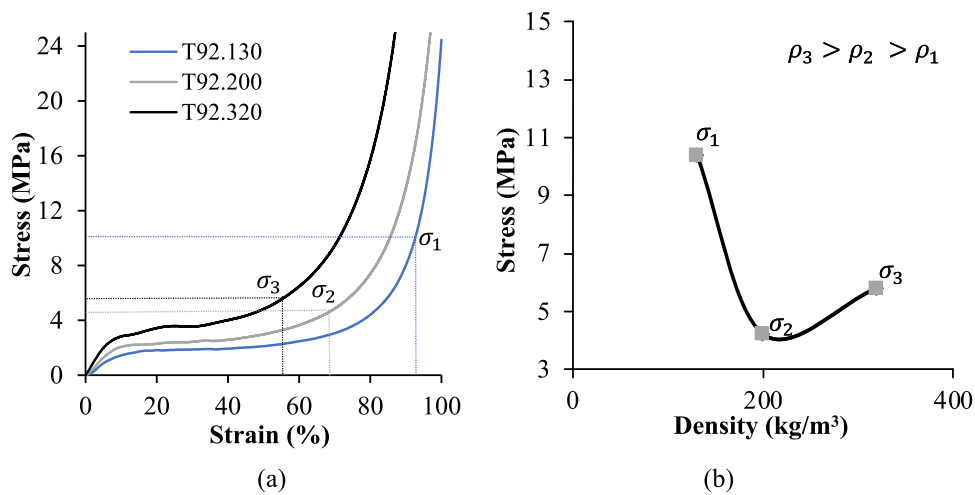
Fig. 5. Stress vs strain diagram (a) Stress-strain curve for the three foams; (b) Peak stress variation at 11.38 J/mm3.

demonstrate that the foam can be impacted by smaller-sized aggregates, up to those larger than the size of the foam's cell. Conversely, aggregates smaller than the cell size of the foam might interact with the foam through the mastic. Moreover, the observed deformation of the energy-absorbing particle in [23] was also caused by smaller aggregates, and given the cell size of these particles, below 0.063 mm, they could be optimised to the smallest size aggregate of the asphalt skeleton; however, the cell sizes of T92.130, T92.200, and T92.320 limit the possibility of optimising the size of the foam without compromising the structural integrity of the cells.
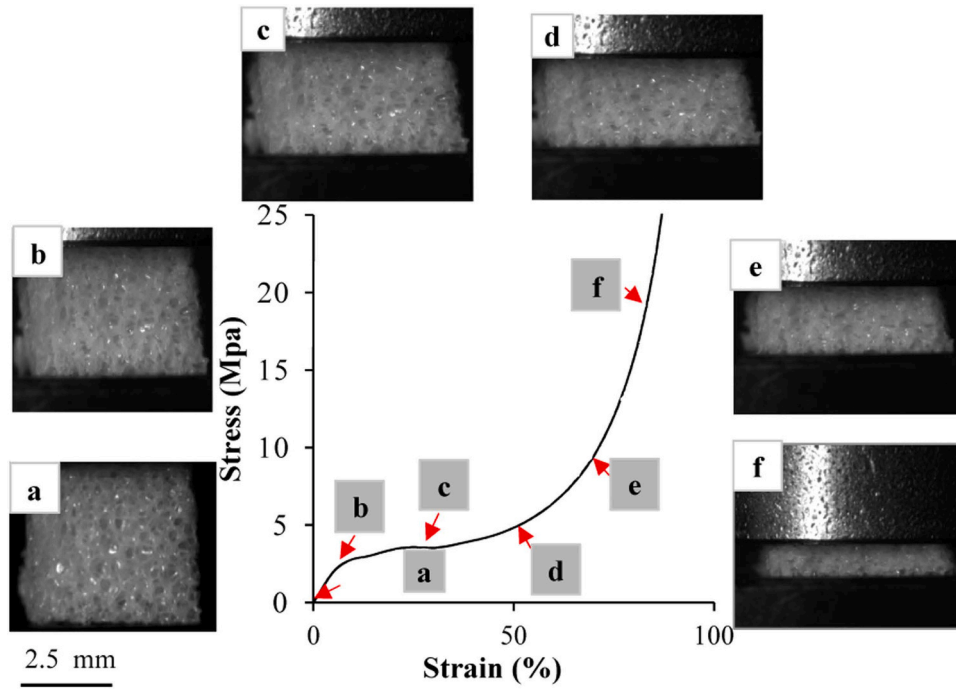
Fig. 6. Stress vs strain curve of T92.200 foam with an illustration of foam damage during the test.
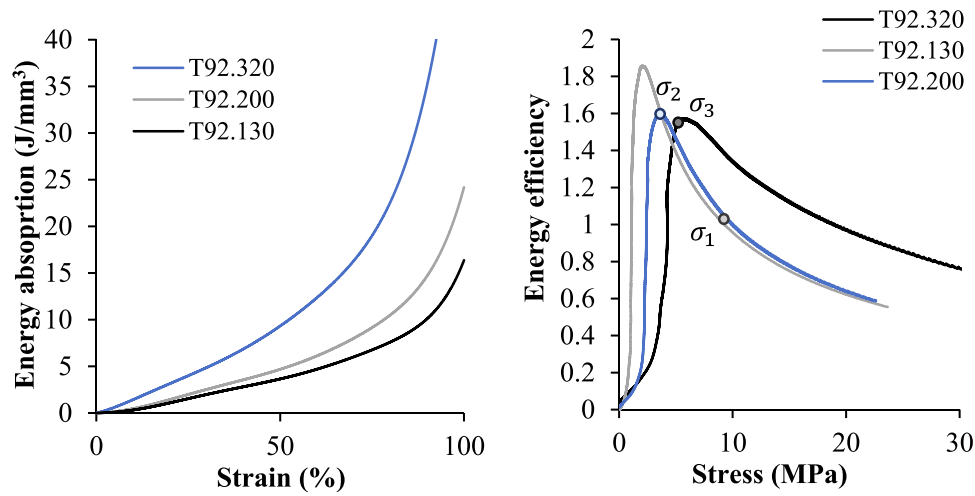
Fig. 7. Energy diagrams (a) energy absorption as a function of strain (b) energy efficiency as a function of stress.

Table 1
Mean value of yield stress, yield strain, elastic modulus, and plateau stress.

Foam type	Loading rate (mm/s)	Yield stress (MPa)	Yield strain (%)	Elastic modulus (MPa)	Plateau stress (MPa)
130	0.5	0.80	5.52		2.76
	0.5			15.2	
200	0.5	2.12	7.79	25.1	3.09
320		2.27	9.97	41.5	4.72

Fig. 8. Aggregate-foam contact.

3.4. Particle loss resistance

Average mass loss results of asphalt cores containing (0 %, 1 %, 3 %, 4 % and 5 % by total weight of asphalt mixture) were tested in a Los Angeles drum. The results with their error bars ± standard deviations are depicted in Fig. 10. Asphalt mixtures without foam presented the
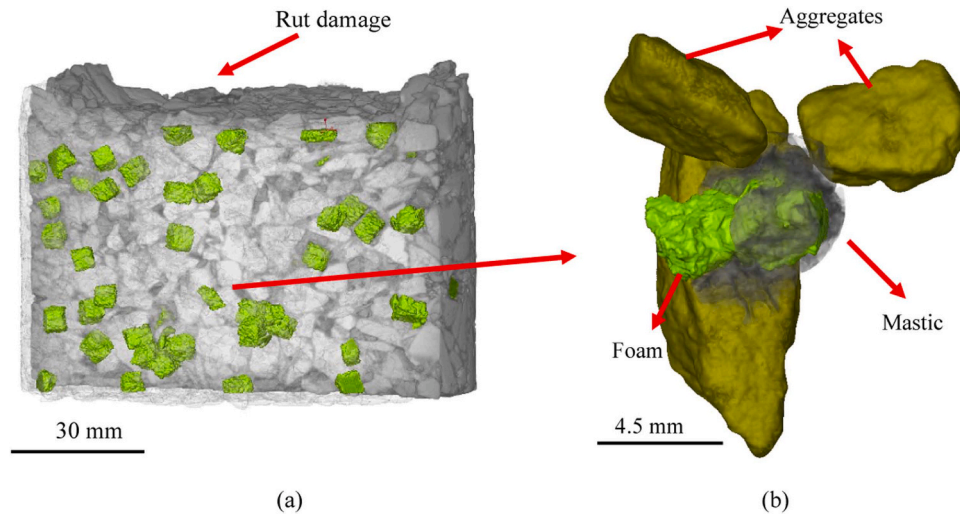
Fig. 9. (a) CT-scan view of tested asphalt core with foam under Hamburg Wheel Tracker (b) Reconstruction of deformed foam and interaction with surrounding aggregates after Hamburg Wheel tracker-test.
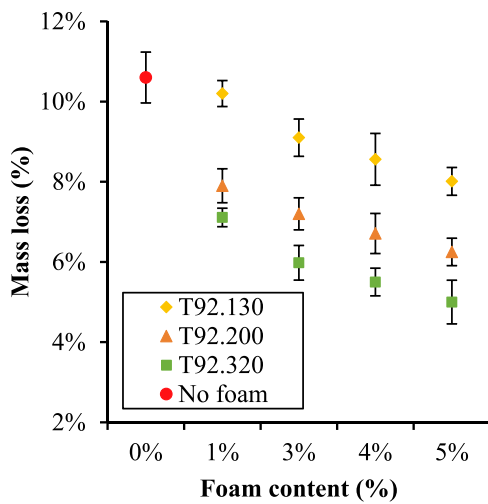
Fig. 10. Particle loss resistance with 5 %, 4 %, 3 %, 1 % and 0 % of T92. Foam.

highest particle loss, around 10.60 %. As foam content increased in the asphalt mixture, the mass loss decreased in the three types of foams. The association between the variables of each foam was modelled by a linear regression, and the goodness of the fit was assessed through the coefficient of determination, which was approximately, 0.9649, 0.9893 and 0.9501 for T92.130, T92.200 and T92.320, respectively. The minimum loss of aggregate was obtained with asphalt cores with T92.320 at the 4 different percentages, followed by T92.200 and T92.130. As can be seen,

there is an inverse relationship between the foam density and particle loss, meaning the higher the foam density, the lower the particle loss. Asphalt cores containing T92.130 exhibited a particle loss reduction of 20 % when the foam concentration was 5 %, whereas 5 % of T92.200 and T92.320 presented around 41.04 % and 52.83 % lower mass loss, respectively, relative to the reference specimen. Based on these findings, the focus of comparison for the remainder of this study was restricted to 1 % and 5 % foam, owing to its limited availability.

To further illustrate the state of the core following the test, images without foam and with various percentages of T92.200 foam were taken to show the asphalt's level of disintegration, see Fig. 11. In comparison, the asphalt without foam exhibited more substantial damage, whereas the one with foam presented reduced damage at the core's surface and edges. The findings derived from the analysis of the images, in conjunction with the inherent characteristics of the foam, indicate that the foams might serve as shock absorbers. This is achieved by the deformation of the foam and the absorption of the kinetic energy from the samples impacting the inner walls of the Cantabro.

The absorbed energy might prevent the aggregate from being detached by enhancing the tensile strength and contributing to the cohesion of the material. In addition, the correlation between the percentage of mass loss and the addition of foam indicates that the hypothesis of energy absorption holds true; increasing the amount of foam would result in a decrease in mass loss. Furthermore, if the asphalt were exclusively composed of foam, the result of the Cantabro test would exhibit a compacted material without any foam loss. Similar results were seen with energy-absorbing particles reported by Traseira et al. [23], whereby the inclusion of these particles in asphalt led to a significant reduction of 30 % in mass loss. It was also observed that the air void content and varying compaction energy significantly influence the
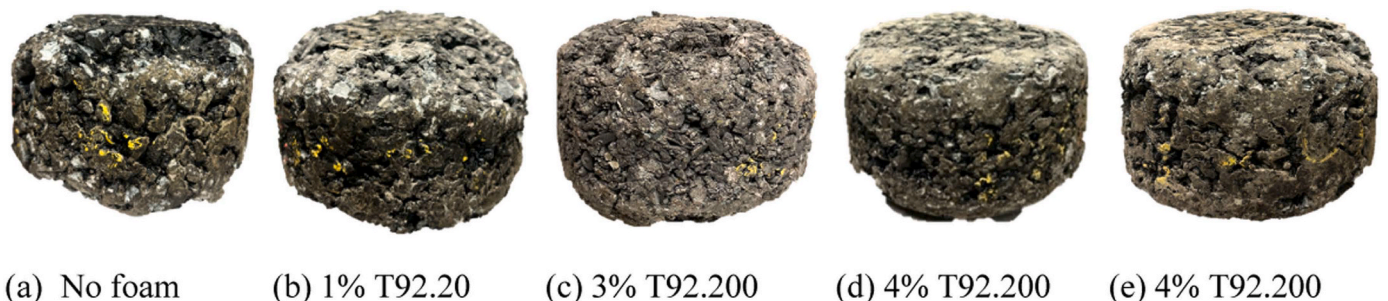
Fig. 11. Asphalt cores with different content of T92.200 foam after 300 cycles in the Cantabro test.

decrease in mass loss of asphalt-containing energy-absorbing particles due to the improved creation of a solid framework that can withstand external loads and give a better energy distribution [23].

3.5. Influence of foam on asphalt volumetric properties

Table 2 represents the average (± 1 standard deviation) of bulk density and air void content measurement of core sample sets containing 0 % 1 % and 5 % of the three foam types. The values were calculated from five tested specimens for each foam type and content level. Results show that the bulk density of compacted cores decreased with adding 1 % and 5 % foam compared to specimens without foam. Air void content for 1 % foam increased by 0.15 %, 0.26 % and 0.34 %, while 5 % foam content exhibited even higher increases of 0.51 %, 0.60 % and 0.61 % for T92.130, T92.200 and T92.320, respectively, as compared to the reference specimens. The addition of foam might have reduced compaction efficiency, likely stemming from the impact of their size and density on the solid skeleton and interlocking properties. This influence might result in modifications of the asphalt matrix and aggregate arrangement compared to those without foam, explaining the increase of air void content. Moreover, a more pronounced increase is observed in T92.200 and T92.320 compared to T92.130, the latter characterised by a lower density and compressive stiffness, enabling the foam to deform slightly more than T92.200 and T92.320, potentially contributing to better compaction.

3.6. Rutting resistance of SMA mixtures

In contrast to mass loss testing, adding foam to asphalt increases the rutting; see Fig. 12. The proportional rut depth evolution over time revealed different asphalt deformation rates for each asphalt containing 1 % and 5 % content of T92 foams. The rut depth of materials with 1 % foam content increased by 10 %, 16 %, and 17 %, registering maximum rut depths of 1.75 mm, 1.95 mm, and 2.08 mm for T92.130, T92.200 and T92.320, respectively. With 5 %, a higher increase occurred of 24 %, 26 % and 32 % with maximum rut depths of 2.29 mm, 2.3 mm and 2.59 mm, see Table 3. However, these values are considered far less than 12.5 mm after 10.000 cycles, considered the maximum allowable rut depth for mixtures using HWTT according to [65], [66]. In addition, according to [67], HWTT is a repeatable test capable of generating good quality data with low variability and acceptable statistical credibility correlated to field performance.

The present findings from the rutting test, volumetrics, and Cantabro tests are related, indicating that the inclusion of these foams affects the arrangement and interlocking of the aggregate. This impact is evident in the air void, which confirms that the foams create a distinct aggregate skeleton. However, the foams are only deformed by external forces, modifying the asphalt rut depth and particle loss.

3.7. Asphalt stiffness

Fig. 13 depicts the results of stiffness modulus of asphalt samples containing 1 % and 5 % foam at 10°C and 20°C, along with their

Table 2
Densities and air void content of asphalt mixtures with 0 %, 1 % and 5 % of T92 foam.

Type of mixture	Theoretical maximum density (kg/m^3)	Bulk density (kg/m^3)	Air void content (%)
Without foam	2551	2411± 0.017	5.50 % ± 0.5
T92.130–1 %	2529	2386 ± 0.005	5.64 % ± 0.3
T92.130–5 %	2436	2290 ± 0.010	6.01 % ± 0.2
T92.200–1 %	2529	2383 ± 0.012	5.76 % ± 0.2
T92.200–5 %	2448	2315 ± 0.018	6.10 % ± 0.4
T92.320–1 %	2530	2333 ± 0.007	5.84 % ± 0.2
T92.320–5 %	2450	2299 ± 0.017	6.11 % ± 0.4
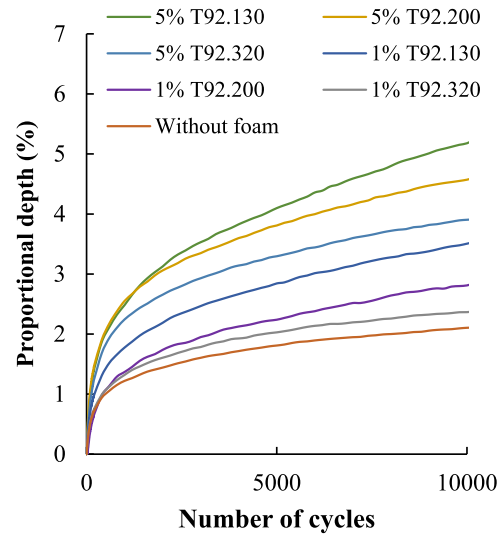
Fig. 12. Rut depth cycles.

Table 3
Summary results of rut depth.

Type of mixture	Proportional rut depth (%)	Wheel track slope in water (mm/1000 load cycles)
Without foam	2.11	0.059
T92.130–1 %	2.38	0.061
T92.130–5 %	2.58	0.066
T92.200–1 %	3.47	0.067
T92.200–5 %	3.89	0.076
T92.320–1 %	4.55	0.089
T92.320–5 %	5.15	0.108
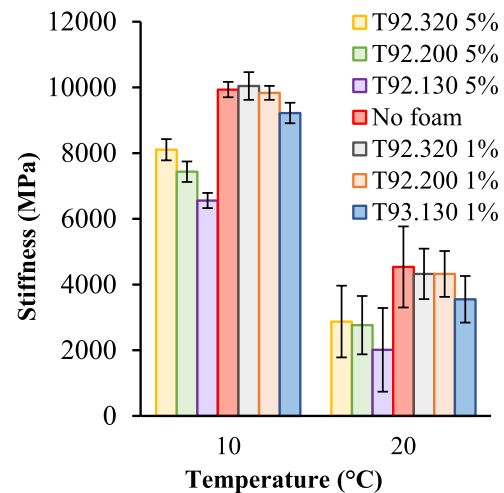
Fig. 13. Stiffness results from ITSM test at two different temperatures with 0 %, 1 % and 5 % of T92 foam.

corresponding error bars. It is evident that asphalt samples with 1 % of any type of T92 foam show average stiffness modulus similar to the control specimens at 10°C and 20°C. However, increasing the foam content to 5 % reduces the stiffness modulus for both tested temperatures. Specifically, at 10°C, the reduction of stiffness of asphalt with 5 % foam content is approximately 33 %, 25 % and 18 % for T92.130, T92.200 and T92.320, respectively. However, the stiffness at 20°C exhibits higher variability among the specimens within each set. From the analysis of ITSM mean values in Fig. 13, it becomes apparent that the

standard deviation is higher at 20°C degrees than at 10°C. This could be attributed to the higher influence of the viscoelastic properties of bitumen on the deformation control during the test conducted at high temperatures [68]. In greater detail, it's possible to observe that graphically, there is no notable variation between ITSM values of asphalt with 5 % of T92.130, T9.200, and T92.320 exhibited at 20°C. However, the increase in foam content clearly impacts on stiffness at both temperatures.

3.8. Fatigue failure

In Fig. 14 (b), the correlation between the deformation and the number of cycles (N) is presented for asphalt specimens containing 0 %, 1 %, and 5 % of the three T92 foams conducted at a stress level of 650 kPa at 10°C. All materials exhibit a similar trend in which their deformation behaviour might be categorised into three distinct regions known as the three-stage law [69] Fig. 14 (a). The first region illustrates a rapid increase of deformation over a small number of cycles attributable to a decrease of air void content and viscoelastic damping [70], [71]. As the cycles progress, the aggregates become more closely packed, leading to a subsequent linear increase in deformation, where microcrack initiation occurs [69]. During the last stage, the microcracks rapidly propagate to macrocracks, exhibiting a higher increase of deformation. These macrocracks eventually result in fatigue failure, at the point where the specimen breaks in half [72], [73], [74].

The impact of the selected stress level of 650 kPa on different asphalt mixtures containing 0 % 1 % and 5 % of T92 foam under indirect tensile testing is graphically illustrated in Fig. 14 (b). When subjected to the same stress level, asphalt without foam in stage A exhibits a higher deformation compared to asphalt with varying foam percentages. In contrast, asphalt samples containing 1 % and 5 % of T92 foam all exhibit a lower strain rate, possibly due to the effect of the foam on the aggregate arrangement and their energy absorption properties, which might manifest at the beginning of the test. This is also corroborated by [75], where the inclusion of designed porous particles proved to have a physical effect on the asphalt aggregate skeleton, ultimately affecting its performance and durability.

Furthermore, there is a correlation between the relative density of the foam and its content in relation to the fatigue life of asphalt. Asphalt containing 1 % and 5 % of T92 showed improved fatigue resistance with greater foam density despite having lower stiffness modulus. Yet, materials without foam, while exhibiting higher stiffness, experience a lower fatigue resistance. One possible explanation could be that the inclusion of energy-absorbing foams might reduce the stresses applied to

the aggregate and the bitumen, thereby slowing down the propagation of cracks. This phenomenon is seen in concrete panels with an integrated layer of polymer foam serving as a layer to spread out concentrated loads and delay cracking [76]. These results may not represent the material fatigue behaviour under all stress conditions. Nonetheless, they give valuable insight into how the material might respond under cyclic tensile stress.

Lastly, after the specimens were broken, several foams were visible, and upon a closer look at the internal section, it is revealed, as seen in Fig. 15 a clean internal section with white surfaces, indicating no bitumen absorption. Fig. 15 (b) illustrates a closer view of an extracted T92.200 foam from the asphalt, showing no signs of bitumen absorption.

3.9. Asphalt ravelling resistance

Previous research investigating the influence of energy-absorbing particles on the mitigation of asphalt ravelling has mostly focused on evaluating unaged asphalt under repeated cycles of impact loading using the Los Angeles machine [22], [23], [77]. However, this test is unlikely to reflect the gradual surface loss of aggregates and mastic and the braking and cornering forces that lead to asphalt ravelling in most practical field conditions [78], [79]. Hence, a scuffing machine has been used in this study to directly quantify asphalt surface loss under the shear stresses induced by a 20° scuffing wheel, simulating in-service loading [56]. Two slabs were manufactured for each asphalt type, each cut in half, resulting in 4 samples per material [80]. This is to examine whether variations in the geometric properties of asphalt surface, which might occur [81], can affect its wear resistance. Visual inspection of each slab revealed no aggregate and mastic segregation on any sample. The cumulative surface mass loss at 30°C after 2800 cycles for each asphalt type is represented in Fig. 15.

Asphalt without T92 foam exhibited higher material loss than with 1 % and 5 % of T92 foam. The minimum loss was attained with 5 % T92.320, showing 84 % lower mass loss than asphalt containing 0 % T92 foam. However, no significant difference in mass loss was observed among the various T92 types and content, as confirmed by a Student's T-test (P > 0.05) and the overlapping of standard deviations for both proportions. Moreover, the analysis of gradual particle loss presented in Fig. 17 (a) shows an accelerated onset of mass loss after the first set of 312 cycles for asphalt containing 0 % T92, in contrast to asphalt containing any type and content of T92 foam, where the initiation occurs after 624 cycles. This observation suggests that the deformation and energy absorption capability of the foam might aid in mitigating the early initiation of aggregate loss from the surface induced by load and
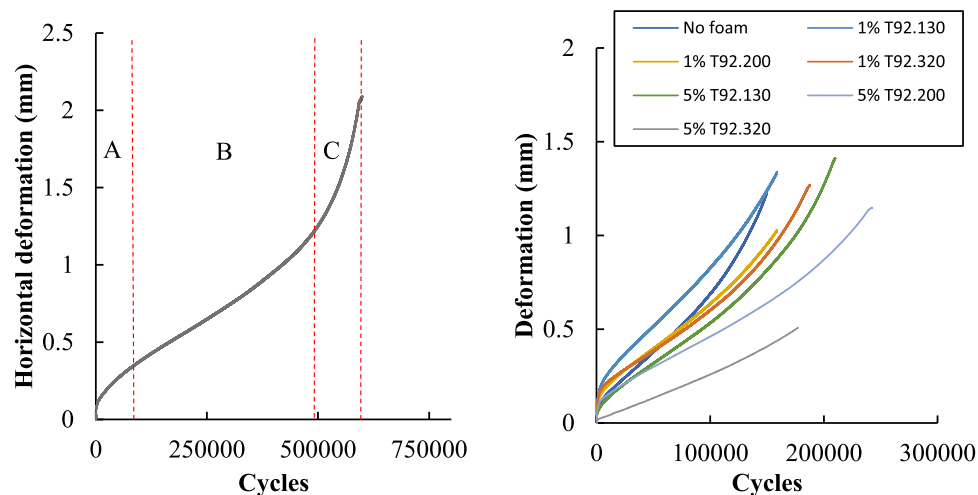
Fig. 14. (a) Schematic relationship between horizontal deformation and number of cycles (b) Indirect tensile fatigue results for different asphalt mixtures containing 0 %, 1 % and 5 % of T92.
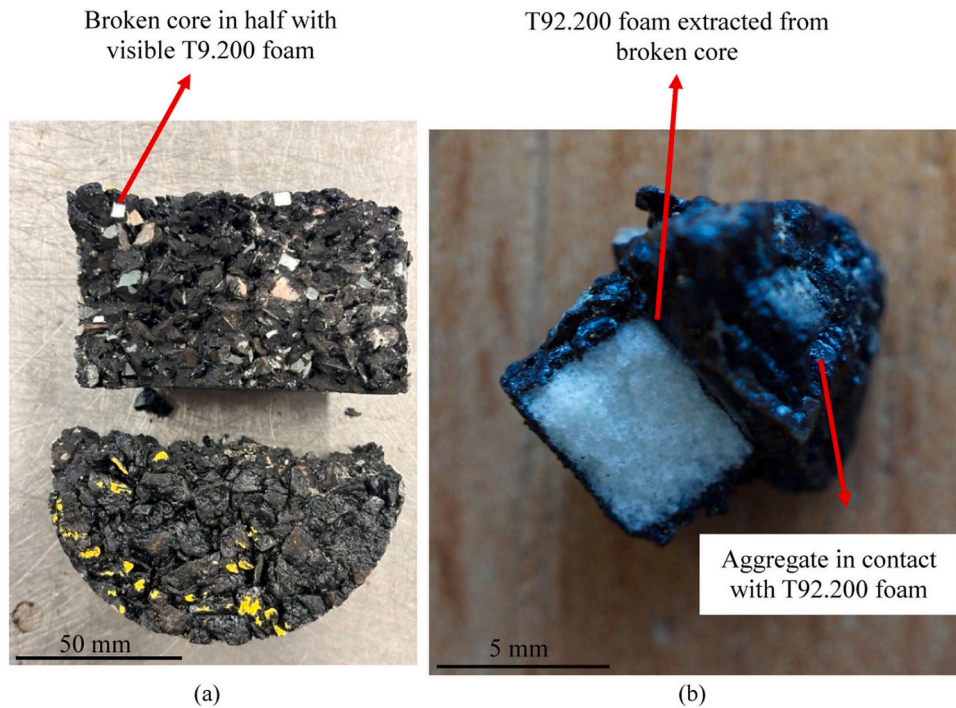
Fig. 15. Illustration of foam internal structure after asphalt manufacturing and testing (a) Asphalt core fractured from fatigue test with visible white and clean surface of T92.200 foam (b) T92.200 foam extracted from damaged core showing the white and clean internal porous structure of the foam.
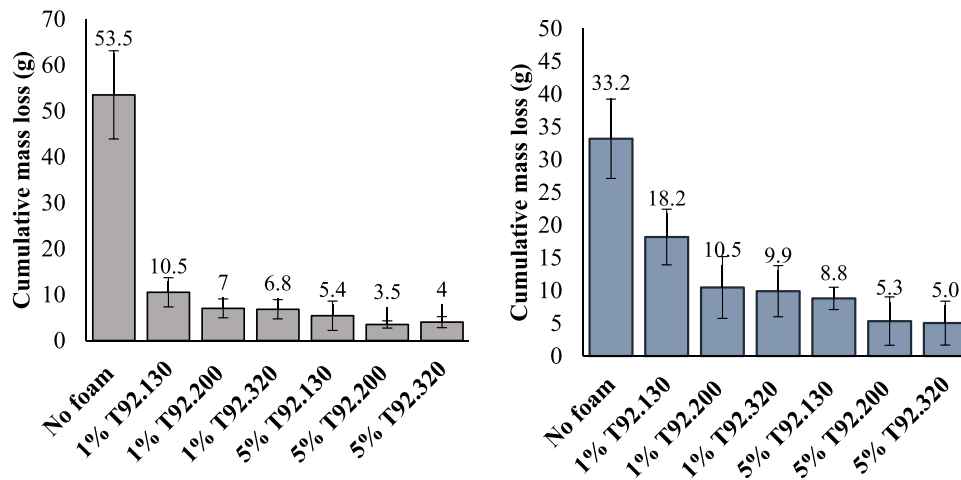
Fig. 16. (a) Cumulative mass loss average from two half specimens of a slab containing 0 %, 1 %, % 5 % of T92 from the first batch of asphalt slab manufacturing (b) Cumulative mass loss average from two half specimens of a slab containing 0 %, 1 %, % 5 % T92 from the second batch of asphalt slab manufacturing.

scuffing wheels. It is hypothesised that the foam's presence aids in absorbing the critical horizontal load that might break the bonds between asphalt components.

Moreover, the progressive macrotexture evolution for one tested slab per material was examined and is presented in Fig. 17, showing a similar degradation trend for all mixes. All mixtures initially exhibited a value ranging from 0.9 to 1.25 mm, which, according to [82], [83] is considered 'very good' for surface macrotexture. After the first set of 312 cycles, all mixtures experienced a drop in the MPD value, which could be attributed to the migration phenomenon of the bitumen inside the voids of the mix [83], [84]. After the first set of cycles, the texture slightly increases again, perhaps resulting from migrated bitumen being removed and the aggregates being more exposed [85]. This implies that there might be a correlation between the mass loss and macrotexture change. However, other studies have explained that this trend might

differ for different mix types, and it also depends on the PSV values of the aggregates [85], [86]. If MPD is used as a metric to assess the early fretting and subsequent ravelling in road surfaces, the dust interposed between the wheel and the surface, combined with climatic conditions, could cause the MPD to fluctuate throughout the year [87]. Therefore, it would be difficult to predict the evolution of ravelling in the road. Nevertheless, it is clear from the values of MPD from the materials without foam that the disintegration of the surface will result in greater texture values.

Images were also taken before and after the test to visually assess the surface condition at the end of the test. As seen in Fig. 18 and Fig. 19. Visual inspections of the slabs revealed higher surface mass loss in material with foam. Wear and abrasion are predominately seen in the middle and edges of the slab.

12
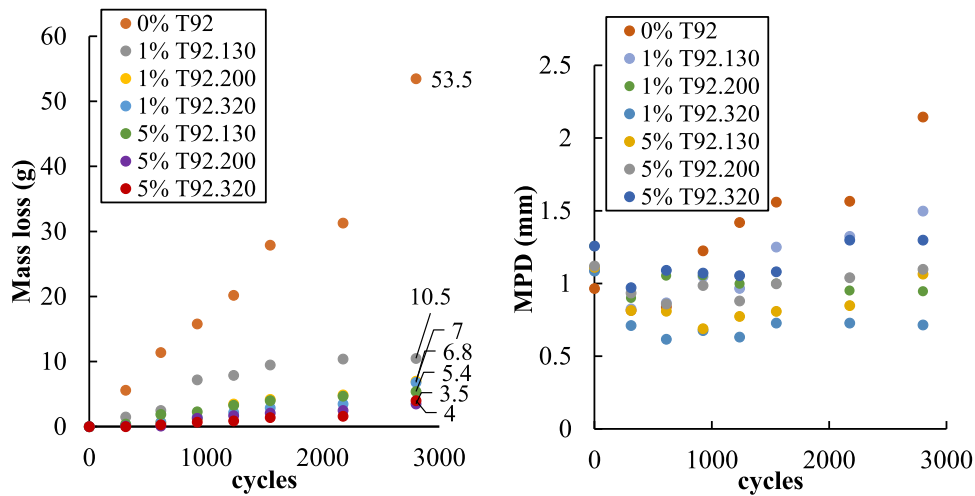
Fig. 17. (a) Mass loss evolution every 312 cycles. (b) Mean Profile Depth (MPD) evolution every 312 cycles.
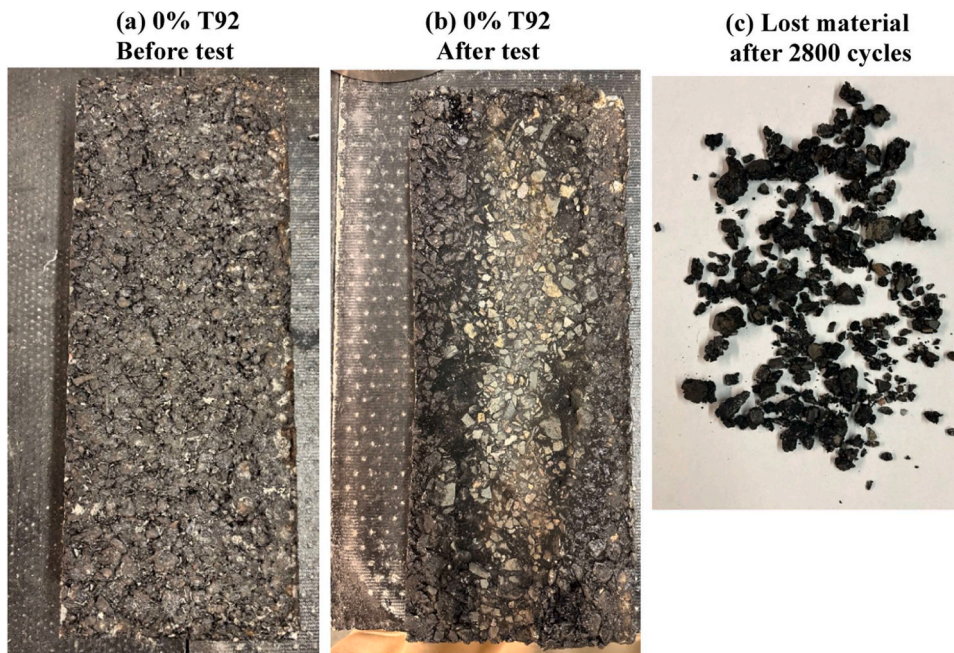
Fig. 18. (a) 0 % T92 asphalt slab image before test (b) after test and (c) Lost material after 2800 cycles.

4. Conclusions

This study has examined the use of PET foam (Airex T92), a commercially available cellular structure, as a possible substitute for energy-absorbing encapsulated particles to enhance asphalt durability. Three foam types were chosen to characterise the material and assess the effect of density and subsequent energy efficiency on the mechanical performance of the asphalt, particularly the impact of their inherent energy absorption characteristics on mitigating asphalt ravelling. Firstly, the foams were examined and classified according to their internal structure. Subsequently, their behaviour was analysed using compression testing to obtain their mechanical properties based on the stress and strain response of each foam. Lastly, two percentages of foam in asphalt were selected based on the Cantabro findings and also due to the constrained availability of the foam coupled with the challenging nature of the cutting process, to further study the volumetrics, rutting, stiffness, fatigue, particle loss and wear resistance. Based on the results of this research, the following conclusions were obtained:

- PET foam with different densities and pore sizes absorbs a given amount of energy at different stress levels. From the efficiency diagram, T92.200 requires lower stress for the same energy absorption.
- CT scan images revealed that T92 foam was 16.5 %-25 % less in volume after asphalt manufacturing. Damaged asphalt from the Hamburg Wheel tracker revealed deformed foams based on the obtained images.
- The addition of foam increased the void content of the mixtures, reducing compaction effectiveness, likely stemming from the impact of their size and density on the solid skeleton and interlocking properties. A more pronounced increase of air void was seen in asphalt mixtures with higher-density foams.
- Asphalt containing 1 %, 3 %, 4 %, and 5 % of the three types of T92 foam showed a linear trend in mass loss in the Cantabro test, with the asphalt without T92 foam exhibiting the highest mass loss. The rutting, on the other hand, was higher for asphalt materials containing T92 foam, with an even greater increase when the content of the foam was increased.

(a) 1% T92.200 Before test   **(b) 1% T92.200 After test**   **(c) Lost material after 2800 cycles**
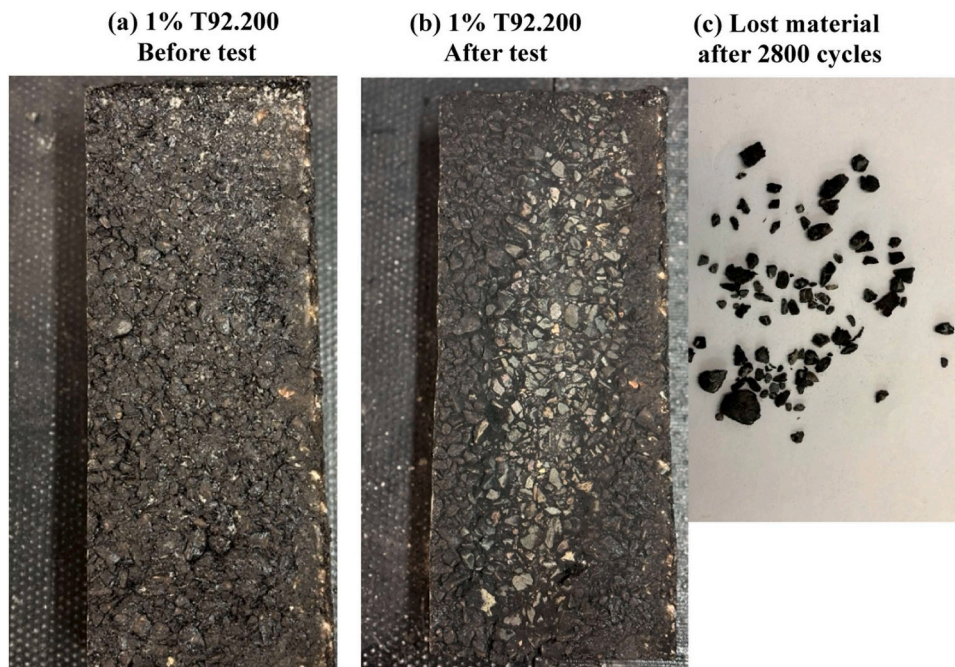
Fig. 19. (a) 1 % T92.200 asphalt slab image before test (b) after test and (c) Lost material after 2800 cycles.

- A correlation was identified between stiffness and fatigue in asphalt compositions containing 0 %, 1 %, and 5 % foam. The number of cycles at which the samples fractured and broke was higher for materials containing 5 % foam; however, asphalt mixtures without foam and with 1 % foam exhibited a comparable fatigue response. This observed trend contrasts with the stiffness behaviour, where stiffness decreases with increasing foam content.
- Surface particle loss tested through the scuffing test showed similar loss for materials containing 1 % and 5 % in contrast to the Cantabro results. Asphalt not containing foam showed much higher mass loss and MPD values compared to asphalt with T92 foam.

5. Limitations and future research

The mechanical behaviour of cellular structures is primally tailored through cell shape, size, and material composition design. However, in this study, the foam influence in asphalt was predominantly studied through the effect of different densities and a porous structure. Consequently, the effect of cell geometry and overall structural design on the mechanical behaviour of asphalt should also be considered, incorporating an approach aimed at tailoring cellular structures to aid in other road performance aspects such as permeability, noise, and skid resistance. In addition, future studies should also evaluate the influence of PET foams on the low-temperature performance and water resistance of asphalt mixtures. Lastly, the foam distribution in asphalt should be further evaluated with additional CT scans, as the difference in densities between the aggregates and foam might cause segregation.

CRediT authorship contribution statement

Nick Thom: Writing – review & editing, Visualization, Supervision. **Mariam Abedraba-Abdalla:** Writing – review & editing, Writing – original draft, Methodology, Data curation, Conceptualization. **Linglin Li:** Writing – review & editing. **A. Garcia-Hernández:** Writing – review & editing, Supervision, Conceptualization.

Declaration of Competing Interest

The authors declare the following financial interests/personal

Data Availability

Data will be made available on request.

References

[1] H. Zhang, K. Anupam, A. Scarpas, C. Kasbergen, S. Erkens, Effect of stone-on-stone contact on porous asphalt mixes: micromechanical analysis vol. 21 (8) (2019) 990–1001, https://doi.org/10.1080/10298436.2019.1654105.

[2] E.R. Brown, H. ManglorkarEvaluation of Laboratory Properties of SMA Mixtures Research Report, 1993.

[3] K. Blazejowski, Stone Matrix Asphalt: Theory and practice, CRC PRESS, 2019.

[4] D. Woodward, P. Millar, C. Lantieri, C. Sangiorgi, V. Vignali, The wear of stone mastic asphalt due to slow speed high stress simulated laboratory trafficking, Constr. Build. Mater. vol. 110 (2016) 270–277, https://doi.org/10.1016/J.CONBUILDMAT.2016.02.031.

[5] E.R. Brown and J.E. Haddock, Method To Ensure Stone-on-Stone Contact in Stone Matrix Asphalt Paving Mixtures, ⟨https://doi.org/10.3141/1583-02⟩, no. 1583, pp. 11–18, Jan. 1997, doi: 10.3141/1583-02.

[6] H.M.B. Miranda, F.A. Batista, M. de Lurdes Antunes, J. Neves, A new SMA mix design approach for optimisation of stone-on-stone effect, Road. Mater. Pavement Des. vol. 20 (sup1) (2019) S462–S479, https://doi.org/10.1080/14680629.2019.1588779.

[7] A. Abouelsaad, G. White, Review of asphalt mixture ravelling mechanisms, causes and testing, Int. J. Pavement Res. Technol. (2021) 1–15, https://doi.org/10.1007/S42947-021-00100-7/FIGURES/7.

[8] L. Mo, M. Huurman, S. Wu, A.A.A. Molenaar, Ravelling investigation of porous asphalt concrete based on fatigue characteristics of bitumen–stone adhesion and mortar, Mater. Des. vol. 30 (1) (2009) 170–179, https://doi.org/10.1016/J.MATDES.2008.04.031.

[9] E.Y. Hajj, N. Morian, G.A.E. Tannoury, S. Manoharan, and P.E. Sebaaly, Impact of lime application method on ravelling and moisture sensitivity in HMA mixtures, ⟨https://doi-org.nottingham.idm.oclc.org/10.1080/10298436.2010.535539⟩, vol. 12, no. 2, pp. 149–160, Apr. 2011, doi: 10.1080/10298436.2010.535539.

[10] L.T. Mo, M. Huurman, M.F. Woldekidan, S.P. Wu, A.A.A. Molenaar, Investigation into material optimization and development for improved ravelling resistant porous asphalt concrete, Mater. Des. vol. 31 (7) (2010) 3194–3206, https://doi.org/10.1016/J.MATDES.2010.02.026.

[11] J. De Visscher, A. Vanelstraete, Ravelling by traffic: performance testing and field validation, Int. J. Pavement Res. Technol. vol. 10 (1) (2017) 54–61, https://doi.org/10.1016/J.IJPRT.2016.12.004.

[12] F. Canestrari, F. Cardone, A. Graziani, F.A. Santagata, H.U. Bahia, Adhesive and cohesive properties of asphalt-aggregate systems subjected to moisture damage, Road. Mater. Pavement Des. vol. 11 (2010) 11–32, https://doi.org/10.1080/14680629.2010.9690325.

[13] M.J. Khattak, G.Y. Baladi, L.T. Drzal, Low temperature binder-aggregate adhesion and mechanistic characteristics of polymer modified asphalt Mixtures, J. Mater. Civ. Eng. vol. 19 (5) (2007) 411–422, https://doi.org/10.1061/(ASCE)0899-1561(2007)19:5(411).

[14] A. Abouelsaad, G. White, Review of Asphalt Mixture Ravelling Mechanisms, Causes and Testing, Nov. 01, in: International Journal of Pavement Research and Technology, vol. 15, Springer, 2022, pp. 1448–1462, https://doi.org/10.1007/s42947-021-00100-7.

[15] E. Schlangen, "Other materials, applications and future developments, RILEM State Art. Rep. vol. 11 (2013) 241–256, https://doi.org/10.1007/978-94-007-6624-2_6/COVER.

[16] A. Garcia, J. Norambuena, R. Micaelo, T. Al MansouriCapsules for asphalt self-healing, Chennai, 2017.

[17] J.F. Su, J. Qiu, E. SchlangenSelf-healing Bitumen by Microcapsules Containing Rejuvenator.

[18] S. Xu, A. García, J. Su, Q. Liu, A. Tabaković, E. Schlangen, Self-healing asphalt review: from idea to practice, Adv. Mater. Interfaces vol. 5 (17) (2018) 1800536, https://doi.org/10.1002/ADMI.201800536.

[19] E.N. Brown, N.R. Sottos, S.R. White, Fracture testing of a self-healing polymer composite, *2002 42:4*, Exp. Mech. vol. 42 (4) (2002) 372–379, https://doi.org/10.1007/BF02412141.

[20] R.C. Barrasa, V.B. López, C.M.-P. Montoliu, V.C. Ibáñez, J. Pedrajas, J. Santarén, Addressing durability of asphalt concrete by self-healing mechanism, Procedia Soc. Behav. Sci. vol. 162 (2014) 188–197, https://doi.org/10.1016/J.SBSPRO.2014.12.199.

[21] T. Al-Mansoori, A. GarcíaCharacterization of polymer capsules used for self-healing asphalt pavements, 2016, doi: 10.1201/9781315643274-130.

[22] N. Ruiz-Riancho, L. Traseira Piñeiro, M. Abedraba Abdalla, A. Garcia, Encapsulated bitumen rejuvenators for reflective cracking and ravelling mitigation, Elev. Int. Conf. Bear. Capacit. Roads Railw. Airfields vol. 2 (2022) 201–209, https://doi.org/10.1201/9781003222897-17.

[23] L. Traseira Piñeiro, T. Parry, F. Haughey, A. Garcia-Hernández, Architected cellular particles to mitigate asphalt stone loss, Constr. Build. Mater. vol. 328 (2022) 127056, https://doi.org/10.1016/J.CONBUILDMAT.2022.127056.

[24] L. Traseira-Piñeiro, T. Parry, F. Haughey, A. Garcia-Hernandez, Performance of plant-produced asphalt containing cellular capsules, Materials vol. 15 (23) (2022), https://doi.org/10.3390/ma15238404.

[25] C. Ouzounis, N. Kyrpides, The emergence of major cellular processes in evolution, FEBS Lett. vol. 390 (2) (1996) 119–123, https://doi.org/10.1016/0014-5793(96)00631-X.

[26] J. Stavans, The evolution of cellular structures, Rep. Prog. Phys. vol. 56 (6) (1993) 733, https://doi.org/10.1088/0034-4885/56/6/002.

[27] S.J. Yeo, M.J. Oh, P.J. Yoo, Structurally controlled cellular architectures for high-performance ultra-lightweight materials, Adv. Mater. vol. 31 (34) (Aug. 2019) 1803670, https://doi.org/10.1002/ADMA.201803670.

[28] L. Gibson, M.F. Ashby. Cellular Solids, second ed., Cambridge University Press, 1997.

[29] M. Tomin, Á. Kmetty, Polymer foams as advanced energy absorbing materials for sports applications—a review, J. Appl. Polym. Sci. vol. 139 (9) (Mar. 2022) 51714, https://doi.org/10.1002/APP.51714.

[30] N. Mills. Polymer Foams Handbook, first ed, Elsevier Science & Technology, San Diego, 2007.

[31] X. Hu, E.M. Wouterson, M. Liu, "Polymer foam technology,", Handb. Manuf. Eng. Technol. (2015) 125–168, https://doi.org/10.1007/978-1-4471-4670-4_23/COVER.

[32] H. Liu, Z.X.C. Chng, G. Wang, B.F. Ng, Crashworthiness improvements of multi-cell thin-walled tubes through lattice structure enhancements, Int J. Mech. Sci. vol. 210 (2021) 106731, https://doi.org/10.1016/J.IJMECSCI.2021.106731.

[33] H.N.G. Wadley, N.A. Fleck, A.G. Evans, Fabrication and structural performance of periodic cellular metal sandwich structures, Compos Sci. Technol. vol. 63 (16) (2003) 2331–2343, https://doi.org/10.1016/S0266-3538(03)00266-5.

[34] A. Slann, W. White, F. Scarpa, K. Boba, I. Farrow, Cellular plates with auxetic rectangular perforations, Phys. Status Solidi (b) vol. 252 (7) (2015) 1533–1539, https://doi.org/10.1002/PSSB.201451740.

[35] B.E. ObiPolymeric Foams Structure-Property-Performance: A Design Guide," Polymeric Foams Structure-Property-Performance: A Design Guide, pp. 1–394, 2017, doi: 10.1016/C2012-0-06136-4.

[36] "AIREX ® T92." [Online]. Available: ⟨www.3ACcorematerials.com⟩.

[37] S. Xu, A. Tabaković, X. Liu, E. Schlangen, Calcium alginate capsules encapsulating rejuvenator as healing system for asphalt mastic, Constr. Build. Mater. vol. 169 (2018) 379–387, https://doi.org/10.1016/J.CONBUILDMAT.2018.01.046.

[38] N. Ruiz-Riancho, A. Garcia, D. Grossegger, T. Saadoon, R. Hudson-Griffiths, Properties of Ca-alginate capsules to maximise asphalt self-healing properties, Constr. Build. Mater. vol. 284 (2021) 122728, https://doi.org/10.1016/J.CONBUILDMAT.2021.122728.

[39] R. Micaelo, T. Al-Mansoori, A. García, and A. Garcia, "Effect of capsules containing sunflower oil on the mechanical behaviour of aged asphalt mixture," 2016, Accessed: Oct. 09, 2023. [Online]. Available: ⟨https://www.researchgate.net/publication/307600937⟩.

[40] T. Al-Mansoori, J. Norambuena-Contreras, R. Micaelo, A. Garcia, Self-healing of asphalt mastic by the action of polymeric capsules containing rejuvenators, Constr. Build. Mater. vol. 161 (2018) 330–339, https://doi.org/10.1016/J.CONBUILDMAT.2017.11.125.

[41] "BS EN 12697-8:2018 - Bituminous mixtures. Test methods - Determination of void characteristics of bituminous specimen." Accessed: May 31, 2024. [Online]. Available: ⟨https://knowledge.bsigroup.com/products/bituminous-mixtures-test-methods-determination-of-void-characteristics-of-bituminous-specimens?version=tracked⟩.

[42] "BS EN 12697-5:2009 Bituminous mixtures. Test methods for hot mix asphalt - Determination of the maximum density." Accessed: May 31, 2024. [Online]. Available: ⟨https://knowledge.bsigroup.com/products/bituminous-mixtures-test-methods-for-hot-mix-asphalt-determination-of-the-maximum-density-1?version=standard&tab=preview⟩.

[43] Z.M. Ariff, Z. Zakaria, A.A. Bakar, M.A.M. Naser, Effectiveness of a simple image enhancement method in characterizing polyethylene foam morphology using optical microscopy, Procedia Chem. vol. 19 (2016) 477–484, https://doi.org/10.1016/J.PROCHE.2016.03.041.

[44] M.G. Almeida, R. Demori, A.J. Zattera, M. Zeni, Morphological analysis of polyethylene foams with post-use material incorporated, Polym. Bull. vol. 59 (1) (2007) 83–90, https://doi.org/10.1007/S00289-007-0745-1.

[45] N. Kumar, P.D. Ukey, V. Francis, R.P. Singh, S. SahuPlastic pellets," Polymers for 3D Printing: Methods, Properties, and Characteristics, pp. 307–323, Jan. 2022, doi: 10.1016/B978-0-12-818311-3.00019-7 .

[46] S. RoncaPolyethylene," Brydson's Plastics Materials: Eighth Edition, pp. 247–278, 2017, doi: 10.1016/B978-0-323-35824-8.00010-4 .

[47] Z.M. Ariff, Z. Zakaria, A.A. Bakar, M.A.M. Naser, Effectiveness of a simple image enhancement method in characterizing polyethylene foam morphology using optical microscopy, Procedia Chem. vol. 19 (2016) 477–484, https://doi.org/10.1016/J.PROCHE.2016.03.041.

[48] D. Weaire, S.T. Tobin, A.J. Meagher, S. Hutzler, Foam morphology, Foam Eng. (2012) 5–26, https://doi.org/10.1002/9781119954620.ch2.

[49] J. Miltz, G. Gruenbaum, Evaluation of cushioning properties of plastic foams from compressive measurements, Polym. Eng. Sci. vol. 21 (15) (1981) 1010–1014.

[50] M. Avalle, G. Belingardi, R. Montanini, Characterization of polymeric structural foams under compressive impact loading by means of energy-absorption diagram, Int J. Impact Eng. vol. 25 (5) (May 2001) 455–472, https://doi.org/10.1016/S0734-743X(00)00060-9.

[51] "Energy – absorption and efficiency diagrams of rigid PUR foams." Accessed: Nov. 22, 2023. [Online]. Available: ⟨https://www.scientific.net/KEM.601.246.pdf⟩.

[52] "BS EN 12697-22:2020 Bituminous mixtures - test methods. Wheel tracking, British Standards Institution - Publication Index | NBS." Accessed: Sep. 06, 2022. [Online]. Available: ⟨https://www.thenbs.com/PublicationIndex/documents/details?Pub=BSI&DocID=329744⟩.

[53] "BS EN 12697-26:2018 - TC | 30 Jun 2018 | BSI Knowledge." Accessed: Sep. 06, 2022. [Online]. Available: ⟨https://knowledge.bsigroup.com/products/bituminous-mixtures-test-methods-stiffness/tracked-changes⟩.

[54] "BS EN 12697-17:2017 Bituminous mixtures. Test methods Particle loss of porous asphalt specimens - European Standards." Accessed: Sep. 06, 2022. [Online]. Available: ⟨https://www.en-standard.eu/bs-en-12697-17-2017-bituminous-mixtures-test-methods-particle-loss-of-porous-asphalt-specimens/⟩.

[55] T. Al-Mansoori, R. Micaelo, I. Artamendi, J. Norambuena-Contreras, A. Garcia, Microcapsules for self-healing of asphalt mixture without compromising mechanical performance, Constr. Build. Mater. vol. 155 (2017) 1091–1100, https://doi.org/10.1016/J.CONBUILDMAT.2017.08.137.

[56] J.C. Nicholls, "TRL Laboratory test on high friction surfaces for highways," Crowthorne, 1997.

[57] A. Hössinger-Kalteis, M. Reiter, M. Jerabek, Z. Major, Overview and comparison of modelling methods for foams, J. Cell. Plast. vol. 57 (6) (2021) 951–1001, https://doi.org/10.1177/0021955X20966329/ASSET/IMAGES/10.1177_0021955X20966329-IMG12.PNG.

[58] M. Nofar, J. Utz, N. Geis, V. Altstädt, H. Ruckdäschel, Foam 3D printing of thermoplastics: a symbiosis of additive manufacturing and foaming technology, Adv. Sci. vol. 9 (11) (2022), https://doi.org/10.1002/ADVS.202105701.

[59] S. Cakir, M. Aycicek, E. Altun, A. Akinci, The effect of foaming agent on mechanical and physical properties of Polypropylene, Mater. Sci. Adv. Compos. Mater. vol. 2 (1) (2018), https://doi.org/10.18063/msacm.v2i1.693.

[60] U. Berardi, J. Madzarevic, Microstructural analysis and blowing agent concentration in aged polyurethane and polyisocyanurate foams, Appl. Therm. Eng. vol. 164 (2020) 114440, https://doi.org/10.1016/J.APPLTHERMALENG.2019.114440.

[61] W. Yamsaengsung, N. Sombatsompop, Effect of chemical blowing agent on cell structure and mechanical properties of EPDM foam, and peel strength and thermal conductivity of wood/NR composite–EPDM foam laminates, Compos B Eng. vol. 40 (7) (2009) 594–600, https://doi.org/10.1016/J.COMPOSITESB.2009.04.003.

[62] G. Wypych, Effect of foaming on physical-mechanical properties of foams, Handb. Foam. Blowing Agents (2017) 195–217, https://doi.org/10.1016/B978-1-895198-99-7.50014-3.

[63] T.A. Schaedler and W.B. Carter, "Architected Cellular Materials," 2016, doi: 10.1146/annurev-matsci-070115-031624.

[64] E. Linul, D.A. Şerban, T. Voiconi, L. Marşavina, T. Sadowski, "Energy - Absorption and efficiency diagrams of rigid PUR foams. in *Key Engineering Materials*, Trans Tech Publications Ltd, 2014, pp. 246–249, https://doi.org/10.4028/www.scientific.net/KEM.601.246.

[65] B.W. Tsai, E. Coleri, J.T. Harvey, C.L. Monismith, Evaluation of AASHTO T 324 hamburg-wheel track device test, Constr. Build. Mater. vol. 114 (2016) 248–260, https://doi.org/10.1016/J.CONBUILDMAT.2016.03.171.

[66] K. Mohanraj, A. Gilliland, and TaghaviGhalesari Abbasali, "High-Performance Thin Overlays Department of Transportation and Texas Department of Transportation." Accessed: Jun. 01, 2024. [Online]. Available: ⟨https://www.fhwa.dot.gov/pavement/tops/pubs/TOPS_HPTO_How_To_Report_508.pdf⟩.

[67] L.F. Walubita, L. Fuentes, A. Prakoso, L.M. Rico Pianeta, J.J. Komba, and B. Naik, "Correlating the HWTT laboratory test data to field rutting performance of in-service highway sections," 2019, doi: 10.1016/j.conbuildmat.2019.117552.

[68] Q. You, J. Ma, X. Liu, An experimentally-based viscoelastic behavior of asphalt mastic at high temperatures, Constr. Build. Mater. vol. 177 (Jul. 2018) 358–365, https://doi.org/10.1016/J.CONBUILDMAT.2018.05.116.

[69] J.M. Read, A.C. Collop, Practical fatigue characterization of bituminous paving mixture, J. Assoc. Asph. Paving Technol. vol. 66 (1997).

[70] X. Luo, R. Luo, R. L. Lytton, Characterization of fatigue damage in asphalt mixtures using pseudostrain energy, J. Mater. Civ. Eng. vol. 25 (2) (2012) 208–218, https://doi.org/10.1061/(ASCE)MT.1943-5533.0000633.

[71] S. Xu, X. Liu, A. Tabaković, E. Schlangen, Experimental investigation of the performance of a hybrid self-healing system in porous asphalt under fatigue loadings, Materials vol. 14 (12) (2021), https://doi.org/10.3390/MA14123415.

[72] N. Sudarsanan, Y.R. Kim, A critical review of the fatigue life prediction of asphalt mixtures and pavements, J. Traffic Transp. Eng. (Engl. Ed.) vol. 9 (5) (2022) 808–835, https://doi.org/10.1016/J.JTTE.2022.05.003.

[73] A.G. Evans, E.R. Fuller, Crack propagation in ceramic materials under cyclic loading conditions, Metall. Trans. vol. 5 (1) (1974) 27–33, https://doi.org/10.1007/BF02642921/METRICS.

[74] A. Modarres, P. Alinia Bengar, Investigating the indirect tensile stiffness, toughness and fatigue life of hot mix asphalt containing copper slag powder, Int. J. Pavement Eng. vol. 20 (8) (2019) 977–985, https://doi.org/10.1080/10298436.2017.1373390.

[75] L. Traseira-Piñeiro, M. Bodaghi, A. Grizi, A. Garcia-Hernandez, G. Albertini, Energy-absorbing particles for enhanced mechanical performance of asphalt's aggregate skeleton, Constr. Build. Mater. vol. 415 (2024) 135055, https://doi.org/10.1016/J.CONBUILDMAT.2024.135055.

[76] T. Sevil Yaman, G. Lucier, Cyclic lateral loading behavior of thin-shell precast concrete wall panels, *2023, Vol. 13, Page 2750*, Buildings vol. 13 (11) (2023) 2750, https://doi.org/10.3390/BUILDINGS13112750.

[77] J. Norambuena-Contreras, E. Yalcin, R. Hudson-Griffiths, A. García, Mechanical and self-healing properties of stone mastic asphalt containing encapsulated rejuvenators, J. Mater. Civ. Eng. vol. 31 (5) (2019), https://doi.org/10.1061/(ASCE)MT.1943-5533.0002687.

[78] G. D'angelo, C. Ojum, I. Widyatmoko, M. Wayman, and A. Khojinian, "Ravelling Resistance of UK Thin Asphalt Surface Course Systems Under a Large-Scale Accelerated Test Method".

[79] J. De Visscher, A. Vanelstraete, Ravelling by traffic: Performance testing and field validation, Int. J. Pavement Res. Technol. vol. 10 (1) (2017) 54–61, https://doi.org/10.1016/j.ijprt.2016.12.004.

[80] R. Vaiana, G.F. Capiluppi, V. Gallelli, T. Iuele, V. Minani, Pavement surface performances evolution: an experimental application, Procedia Soc. Behav. Sci. vol. 53 (2012) 1149–1160, https://doi.org/10.1016/J.SBSPRO.2012.09.964.

[81] S. Chen, et al., A state-of-the-art review of asphalt pavement surface texture and its measurement techniques, J. Road. Eng. vol. 2 (2) (2022) 156–180, https://doi.org/10.1016/j.jreng.2022.05.003.

[82] C.R. Bennett *et al.*, "Data Collection Technologies for Road Management Version 2.0-February 2007 East Asia Pacific Transport Unit Data Collection Technologies for Road Management 2 August 2007," 2007.

[83] Alfred, "Performance Indicators for Road Pavements COST 354 Collection of existing basic information WP1 Report Collection of existing basic information Report," 2008.

[84] S. Mcrobbie, C. Wallbank, K. Nesnas, A. Wright, Use of high-resolution 3-D surface data to monitor change over time on pavement surfaces Research into pavement surface disintegration, Phase 3 (2015).

[85] D. Woodward, A. Woodside, R. Ellis, P. Phillips, I. Walsh Jacobs, and U. Ramesh Sinhal, "The effect of aggregate type and size on the performance of thin surfacing materials".

[86] D.J. Wilson, R. Charles, and M. Dunn, "Polishing aggregates to equilibrium skid resistance," 2005. [Online]. Available: ⟨https://www.researchgate.net/publication/228564503⟩.

[87] S. Zhu, X. Ji, Z. Zhang, D. Shao, H. Li, C. Yun, Evolution characteristics of the surface texture of the wearing course on asphalt pavement based on accelerated pavement polishing, Constr. Build. Mater. vol. 333 (2022) 127266, https://doi.org/10.1016/J.CONBUILDMAT.2022.127266.